Interface-related deformation phenomena in metallic glass/high entropy nanolaminates

Q. Xu [a], D. Şopu [a,b,*], X. Yuan [a], D. Kiener [c], J. Eckert [a,c]

[a] Erich Schmid Institute of Materials Science, Austrian Academy of Sciences, Jahnstraße 12, Leoben A-8700, Austria
[b] Institut für Materialwissenschaft, Fachgebiet Materialmodellierung, Technische Universität Darmstadt, Otto-Berndt-Straße 3, Darmstadt D-64287, Germany
[c] Department of Materials Science, Chair of Materials Physics, Montanuniversität Leoben, Jahnstraße 12, Leoben A-8700, Austria

ABSTRACT

The deformation behavior of metallic glass (MG)-high entropy alloy (HEA) nanolaminate is explored through molecular dynamics simulations using nanolaminate models of $FeCoCrNiAl_{1.7}$ MG and $FeCoCrNiAl_{0.5}$ HEA. Quantitative analysis of the atomic strain and dislocation dynamics among competing and cooperative deformation mechanisms is accomplished through the implementation of uniaxial tensile deformation. The combination of glassy and crystalline nanolayers biases the plastic deformation to regions near the glass-crystalline interface at lower strains, which lowers the activation barrier for the onset of dislocation nucleation and propagation. With increasing applied strain, dislocations are absorbed into the amorphous plate via slip transfer across the glass-crystalline interface, in turn triggering the activation of homogeneously distributed shear transformation zones (STZs) in amorphous plate. The competitive deformation mechanism suppresses the formation of localized shear bands and increases the resistance to dislocation motion, thereby promoting enhanced ductility in MG-HEA nanolaminates. Additionally, due to the high strength of the HEA, the laminate structures exhibit a much higher strength than conventional MG-crystalline laminates. The combination of high strength HEAs and MGs and the complex deformation behavior may overcome the typical strength-ductility trade-off and make MG-HEA laminates promising candidates for a variety of structural and functional applications.

1. Introduction

High-entropy alloys (HEAs) have attracted enormous attention over the past decades due to their excellent properties as functional and structural materials in many fields [1–3]. Because of their unique multi-principal element compositions and single crystalline solid solution phase, HEAs possess remarkable properties such as high strength/hardness, high ductility, outstanding wear resistance and exceptional high-temperature strength [4,5]. Therefore, they are used in critical applications, such as aerospace materials, damage resistance materials, tool materials, coating materials, and brazed filler materials [6,7]. Especially, acting as reinforcement in composites, the HEAs with special properties have unique advantages on enhancing the performance of composites [8]. The Al-CoCrFeNiTi HEA with single-crystalline microstructure was used to effectively improve the mechanical properties of Al-Si alloy [9]. The

elastic modulus, tensile strength and elongation of Cu-based composites were enhanced due to the addition of AlCoNiCrFe HEA [10]. Similarly, also the strength and the elongation of an Al-Cu-Ti alloy were improved simultaneously through the addition of AlCrCoFeNi HEA [11].

Similarly, metallic glasses (MGs) possess superior physical, chemical and mechanical properties such as high strength and hardness [12]. In addition, both, HEAs and MGs, are two material classes based on substantial mixing of multi-principal elements. However, the plastic deformation of MGs is highly localized in narrow shear bands (SBs) that promote premature fracture [13–16]. So far, to avoid early failure of MGs, MGs matrix composites with crystalline secondary phases have been synthesized [17–22]. Hereby soft crystalline inclusions act as initiation sites for SBs and effectively distribute the applied strain. Additionally, a number of experimental and computational studies have suggested that multilayered glass-crystalline nanolaminates show outstanding mechanical properties and homogeneous plastic strain [23–30]. The design concept of glass-crystalline nanolaminates, which systematically controls the volume fraction and the thickness of

* Corresponding author at: Erich Schmid Institute of Materials Science, Austrian Academy of Sciences, Jahnstraße 12, Leoben A-8700, Austria.
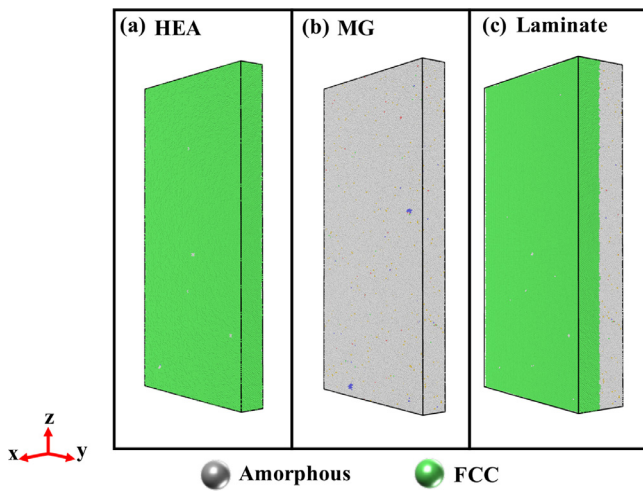*E-mail address:* daniel.sopu@oaew.ac.at (D. Şopu).

Fig. 1. Atomic configurations of (a) HEA, (b) MG and (c) MG-HEA laminate model.
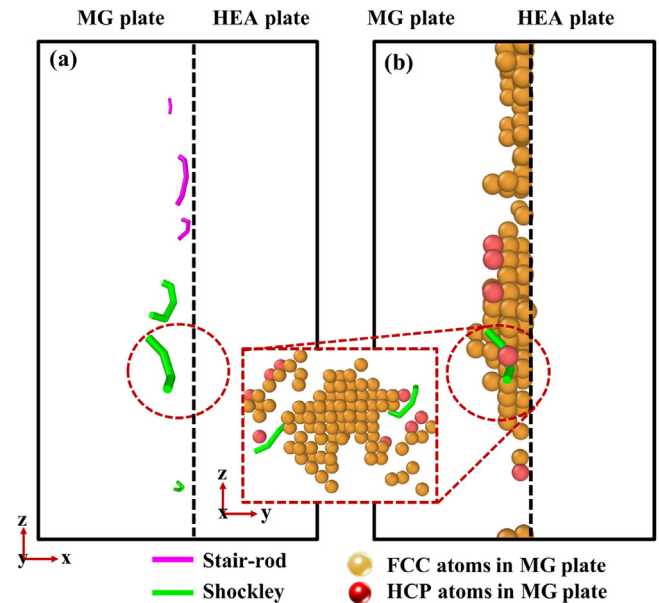

Fig. 2. The dislocation distribution (a), and the microstructure (b) of MG-HEA laminate at the glass-crystalline interface (dashed line). The dashed circle highlights an area of crystallization in the glass plate accompanied by dislocation nucleation. The inset panel displays a different perspective of the same areas marked by the dashed circle.

their component layers, provides a suitable strategy towards the strength-ductility synergy [31–34]. The co-deformation of glass and crystalline phases and the complex interaction between dislocations and SBs through the glass-crystalline interface play a significant role for reaching enhanced mechanical performance [19,35–38]. One therefore wonders if replacing soft crystalline phases with exceptionally strong HEAs may result in novel glass-crystalline nanolaminates that may overcome the strength-ductility trade-off.

In order to provide an atomistic understanding of the co-deformation mechanisms in such laminate structures, we model uniaxial tension deformation of FeCoCrNiAl$_{1.7}$ MG-FeCoCrNiAl$_{0.5}$ HEA nanolaminate using molecular dynamics (MD) simulations in this work. First, the microstructure of the glass-crystalline interface in the MG-HEA laminate is analyzed. Second, the deformation behavior of the nanolaminate is compared to the free-standing HEA plate while dislocation motion and density are monitored. We also differentiate between the deformation behavior of a free-standing MG and the MG plate in the nanolaminate to reveal the confinement effects of the crystalline structure in SB dynamics. Finally, the competing deformation mechanisms in the MG-HEA laminates are investigated with special attention devoted to the glass-crystal interface and the mechanistic coupling of dislocations and SBs.

2. Simulation approach

2.1. HEA, MG and laminate models

In order to understand the co-deformation mechanism in MG-HEA nanolaminates, the uniaxial tensile simulations were performed using the large-scale molecular dynamics simulation package LAMMPS [39]. As shown in Fig. 1, atomic models were created to study the deformation mechanism in HEA, MG and the laminate structure. The atomic interactions were described by the Fe-Co-Cr-Ni-Al embedded atom method (EAM) potential developed by Farkas et al. [40]. The phase structure of FeCoCrNiAlx changes from FCC to BCC and even to an amorphous phase with increasing Al content [41,42]. Hence, we obtained high entropy metallic glasses by increasing the content of Al in the FeCrCoNiAl alloy. The alloy composition of the HEA is FeCoCrNiAl$_{0.5}$ while the one of the MG is FeCoCrNiAl$_{1.7}$. The MG is stable and retains the glassy structure during annealing at elevated temperatures close to T_g ($\approx$ 850 K). For all simulations, a constant integration time step of 1 fs was used. First, the HEA sample was constructed with a simulation box 5 × 30 × 60 nm^3 containing 809,200 atoms and using periodic boundary conditions (PBC). The atoms in the FeCoCrNiAl$_{0.5}$ HEA

are distributed randomly in a FCC crystal structure with a lattice constant equal to 0.35 nm. The crystallographic orientation of the initial configuration of the HEA is x (1 0 0), y (0 1 0), and z (0 0 1), respectively. The HEA sample was prepared following two stages: (1) The system was heated at a rate of 1 K/ps from 50 K to 2000 K, and relaxed at 2000 K for 1 ns. (2) The melt was fast quenched at a cooling rate of 1 K/ps from 2000 K to 50 K and relaxed at 50 K for another 1 ns. The isobaric-isothermal (NPT) ensemble was adopted to simulate the heating and quenching processes.

The FeCoCrNiAl$_{1.7}$ MG sample containing 790,272 atoms randomly distributed in the simulation box of same size as the box used for the HEA plate was produced with PBC in all three directions by quenching from the melt. The MG preparation followed 4 steps: (1) The structure was relaxed at 2000 K for 1 ns to ensure chemical homogeneity. (2) The melt was fast quenched to 800 K, which is 50 K below T_g ($T_g \approx$ 850 K) using a cooling rate of 1 K/ps. (3) The sample was annealed at 800 K for an extended simulation time of 20 ns to better relax the glassy structure. (4) Afterwards, the glass was quenched to 50 K at a cooling rate of 1 K/ps and then relaxed at 50 K for 1 ns. During quenching the system was relaxed in the x-direction (normal to the interface of the MG-HEA laminate) while holding the y- and z-directions fixed to keep the same dimensions as the HEA plate [43,44]. Although the glassy and crystalline plates have the same size in y- and z-directions there are some small residual stresses in these two directions of the MG plate due to the effect of constrained thermal contraction (the system is not allowed to contract on the y- and z-directions). However, the stress components are below 0.1 GPa.

At last, the MG-HEA laminate was constructed by overlapping the model of FeCoCrNiAl$_{1.7}$ MG plate on top of the FeCoCrNiAl$_{0.5}$ HEA plate along the x-direction. The size of the MG-HEA laminate is about 10 × 30 × 60 nm^3 and contains 1,599,472 atoms.

2.2. Uniaxial tensile deformation

To study the mutual deformation mechanisms, the HEA, high entropy MG and MG-HEA laminate samples were deformed at a constant engineering strain rate of 4 × 10^7/s at 50 K along the
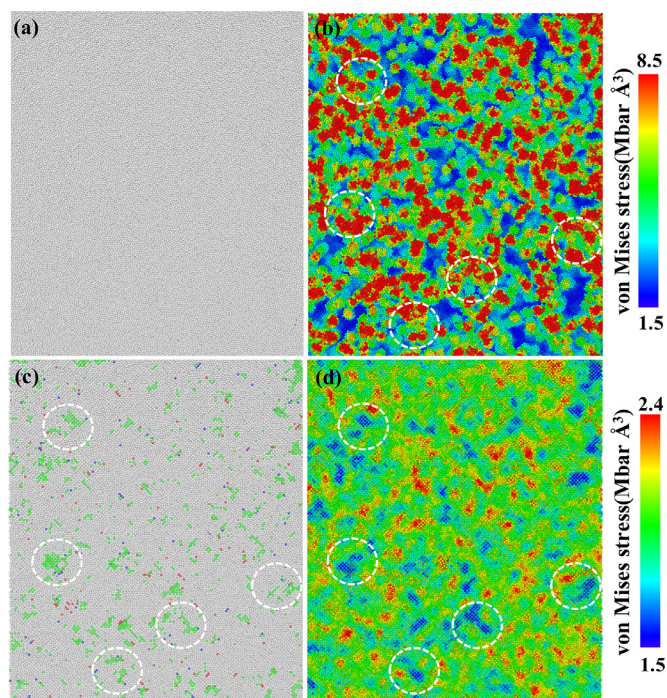
Fig. 3. The microstructure of the MG plate and the stress distribution at the interface of the MG-HEA laminate before relaxation (a), (b) and after relaxation (c), (d). The dashed circles highlight the areas of highest stresses that drive crystallization of the glass. Crystallization induces local stress relaxation. The green areas represent FCC atoms while atoms of the glassy phase are colored in gray. (For interpretation of the references to color in this figure legend, the reader is referred to the web version of this article.)

z-direction. PBC were applied in all three directions. The temperature of the systems is controlled at 50 K within an NPT ensemble, so that thermal effects can be eliminated. Prior to deformation, the samples were relaxed at zero pressure for 1 ns and 50 K to reach an equilibrium state. The visualization software (OVITO) was used to perform the post-processing via Common Neighbor Analysis (CNA), Dislocation Analysis (DXA) and atomic strain to analyze the atomic-scale deformation mechanisms [45–48].
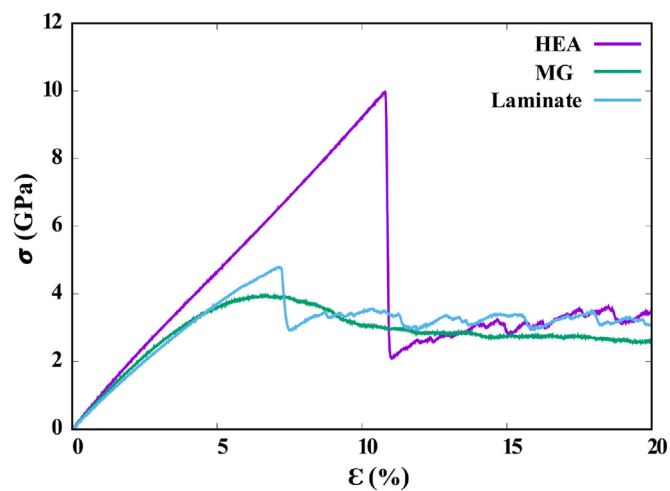

Fig. 4. The tensile stress-strain curves of HEA, MG and MG-HEA laminate, respectively.

3. Microstructure of the glass-crystalline interface in MG-HEA laminate

For the case of laminate structures the interface microstructure and behaviour play a key role in controlling their plasticity. Hence, we also analyze the structure of our model MG-HEA laminate using the DXA and CNA (see Fig. 2). Even before loading, the microstructure at the interface exhibits already large fluctuations. Short Shockley partial dislocations and stair-rod dislocations exist at the glass-crystalline interface (see Fig. 2(a)). The nucleation of these short dislocations at the glass-crystalline interface correlates to the partial crystallization of the glass plate. The weak bonding at the interface and, the correspondingly lower activation energy for crystallization, together with the residual stresses drive atomic rearrangements which leads to crystallization and formation of nanocrystallites distributed along the interface [49]. To better visualize the defects at the interface, all atoms in the system are deleted leaving only those glassy atoms that crystallize (Fig. 2(b)). Most of the atoms crystalize in a FCC structure, but also HCP atoms can be observed. Thus, the defects at the glass-crystalline interface formed before loading, originating from the crystallization of the glassy phase.
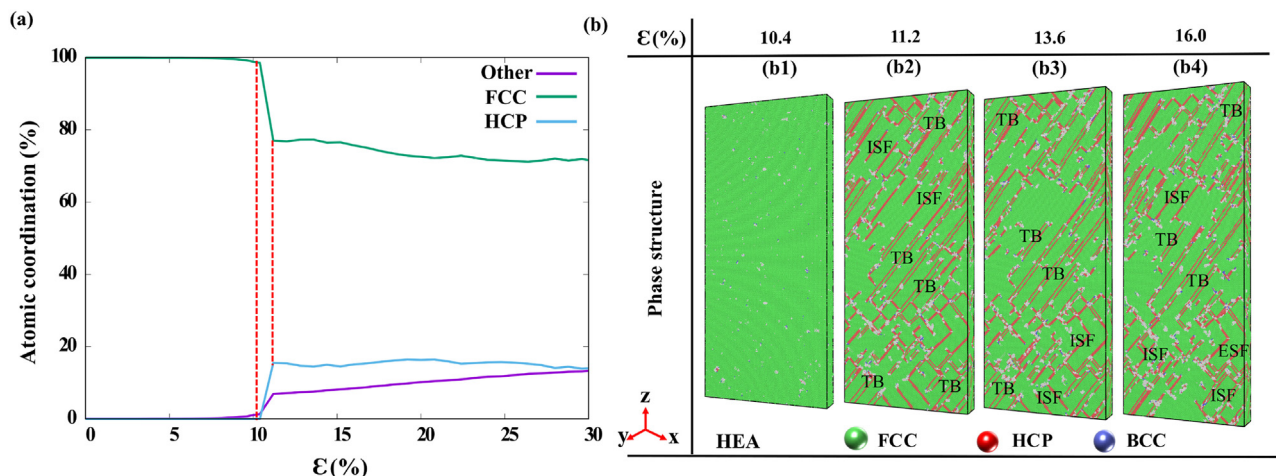

Fig. 5. (a) Fraction of atoms with different lattice structure to the total number of atoms during uniaxial tension of the free-standing HEA. (b) Microstructure of the HEA at different strain levels of (b1) 10.4%, (b2) 11.2%, (b3) 13.6%, (b4) 16%.
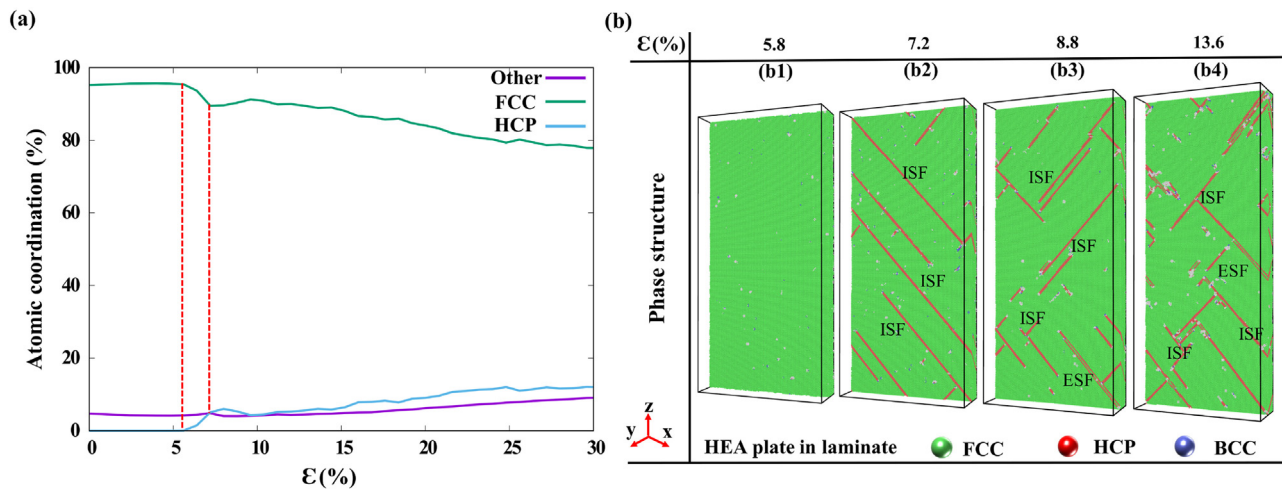
(a)

(b)

Fig. 6. (a) Fraction of atoms with different lattice structure to the total number of atoms during uniaxial tension of the crystalline plate in the laminate. (b) Microstructure of the crystalline plate in the laminate at different strains of (b1) 5.8%, (b2) 7.2%, (b3) 8.8% and (b4) 13.6%. The atoms of the amorphous phase were removed to better visualize the deformation behavior in the HEA plate.
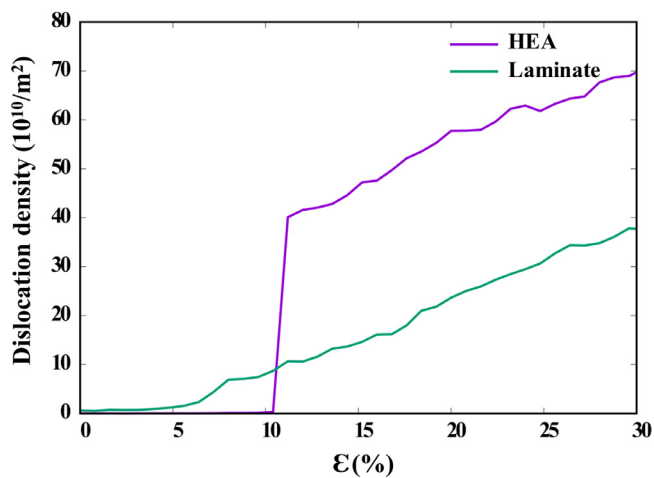

Fig. 7. Dislocation density, defined as the ratio of the total dislocation line length and the crystal cell volume, of the free-standing HEA plate and the HEA plate in the MG-HEA laminate.

The crystallization is an important question that we address next. Fig. 3 displays the microstructure and the stress distribution in the MG plate at the interface before and after relaxation. Before relaxation the microstructure is fully amorphous (see Fig. 3(a)). Moreover, the stress distribution in the glassy plate at the interface is highly inhomogeneous and shows a higher magnitude as compared to the inner part of the glassy plate (Fig. 3(b)). However, after relaxation the stress magnitude decreases while crystallization in the MG plate occurs at the areas of highest stresses (see Fig. 3(c) and (d)). This indicates that high stresses drive atomic rearrangements, which leads to crystallization and formation of nano-crystallites distributed along the interface [49–52]. The crystallization and the related local volume reduction induce local stress relaxation (areas marked with dashed circles in Fig. 3(d)). Thus, the initial residual stress at the glass-crystalline interface leads to local atomic rearrangements and crystallization together with dislocation nucleation even before tensile deformation.

4. Macroscopic deformation mechanisms

Fig. 4 shows the uniaxial tensile stress-strain curves of HEA, MG and MG-HEA nanolaminate. For the HEA, the stress increases lin-

early with increasing the applied strain in the elastic stage ($\varepsilon <$ 10.4 %). The Young's modulus (E) is the slope of the straight-line regime of the stress-strain curve. Here, the Young's modulus of the FeCoCrNiAl$_{0.5}$ HEA is about 97.8 GPa. The theoretical strength (σ_{th}) of a material is often approximated as:

$$\sigma_{th} \simeq \frac{E}{10} = 9.78 \text{ GPa.} \tag{1}$$

This value is closer to the highest stress value of 9.95 GPa at the yield point when the stress undergoes a sudden drop (Fig. 4). Since our system is a perfect single crystal, free of defects, the theoretical strength can be attained [53]. For the FeCoCrNiAl$_{1.7}$ high entropy MG, the ultimate strength is 4 GPa and the Young's modulus is lower than for the HEA ($\approx$ 85 GPa). The stable flow stress is around 2.7 GPa. For the MG-HEA laminate, yielding occurs at a lower strain level ($\varepsilon = 7.2$ %) than for the HEA, suggesting that the glassy plate may control the yielding. Besides, the ultimate strength of the laminate is slightly higher than that of the MG but much lower as compared to the value of the HEA. Furthermore, the strain level at which the stress drops and the magnitude of the stress reduction are lower than for the HEA plate. Hence, the mechanical performance of the MG-HEA laminate cannot be predicted by a simple rule-of-mixtures but special attention should be devoted to confinement effects and interface-related deformation phenomena.

5. Confinement effects in MG-HEA laminates

5.1. Deformation mechanism of the HEA

Next, we differentiate between the deformation behaviors of the free standing MG and HEA systems and their laminate structure and reveal the confinement effects. The deformation mechanism of HEAs under uniaxial tensile loading is dominated by dislocation interactions and movement, which is related to the nucleation and emission of dislocations. In order to study in comparison the microstructure evolution of the free-standing and the confined HEA, the fraction of atoms with different lattice structure as a function of the strain and atomic structures during tensile are shown in Fig. 5. According to the local crystalline classification visualized by CNA, different atomic structures can be distinguished. Green, blue and red colors represent the FCC, BCC and HCP atoms, respectively, while gray color stands for disordered atoms that are not identified as any kind of fundamental atomic structures. The
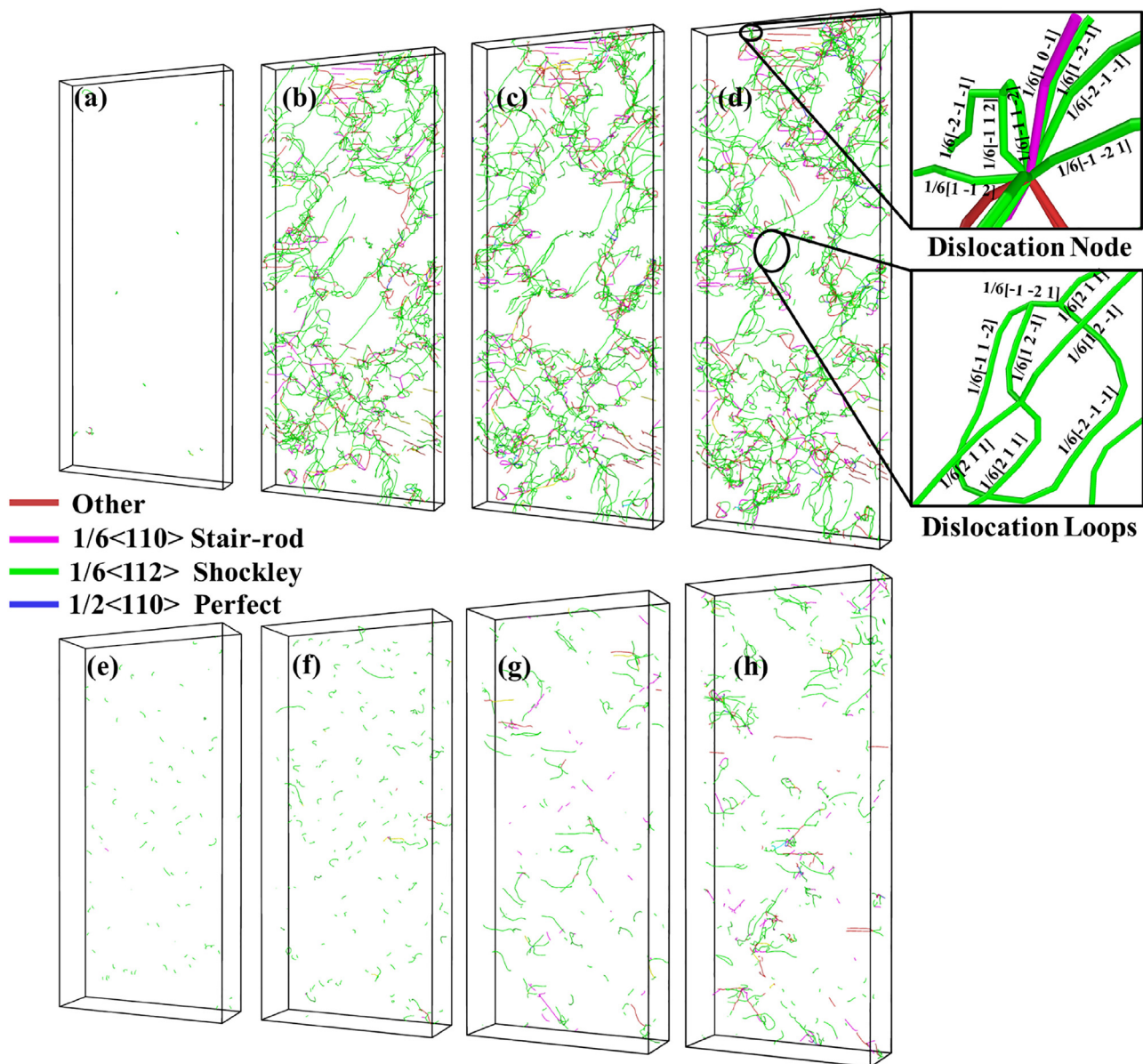
Fig. 8. Dislocation evolution in the HEA under different strains of (a) 10.4%, (b) 11.2%, (c) 13.6%, (d) 16%. Dislocation evolution of the crystalline plate in the laminate under different strains of (e) 5.8%, (f) 7.2%, (g) 8.8%, (h) 13.6%. The magnifications of a dislocation node and dislocation loops, and the Burgers vectors of different dislocation lines in (d) are also displayed.

layered atoms with HCP and FCC structures exhibit different arrangements: a single HCP atomic layer represents a twin boundary (TB), two adjacent HCP atomic layers denote an intrinsic stacking fault (ISF) and two HCP layers with an FCC atomic layer between correspond to an extrinsic stacking fault (ESF) [54]. The fraction of atoms with different atomic coordination during deformation is shown in Fig. 5(a). At yielding, the fraction of atoms with HCP coordination increases due to the formation of intrinsic stacking faults. In the elastic deformation stage there is no defects (see Fig. 5(b1)). With increasing applied strain, the fraction of atoms with HCP and other lattice structures have a sudden increase in the free-standing HEA at a yield strain of 10.4% (Fig. 5(a)). As shown in Fig. 5(b2), an arrangement of ISF and TB forms when the strain increases to 11.2%. This indicates that the formation of SFs and twining is the inherently controlling the yielding of the HEA, that is in good agreement with previous research [55,56]. Also, during yielding, the increase in the disordered atomic configuration indicates

that severe plastic deformation occurs in the free-standing HEA (see Fig. 5(a), (b3) and (b4)).

In case of the laminate, the structure of the HEA plate shows even stronger variations with increasing tensile strain (see Fig. 6). In order to analyze the structure evolution in the crystalline plate, all atoms of the MG in the laminate were deleted. The laminate start yielding earlier and hence, the phase transformation from FCC to HCP structure occurs at a lower strain level of 5.8% (see Fig. 6(a)). Moreover, the fraction of FCC phase that transforms to HCP is nearly a quarter of that found in case of the free-standing HEA plate, while less slip events are activated in the HEA plate in the laminate. Besides, only stacking faults (ISFs and ESFs) form upon deformation, as shown in Fig. 6(d2)–(d4). Due to the confinement effects in the laminate structure the deformation behavior of the crystalline plate changes from twining to ISF formation [57,58]. The activation of deformation twinning requires a relatively high stress or a high strain rate [59,60]. Nevertheless, the partial
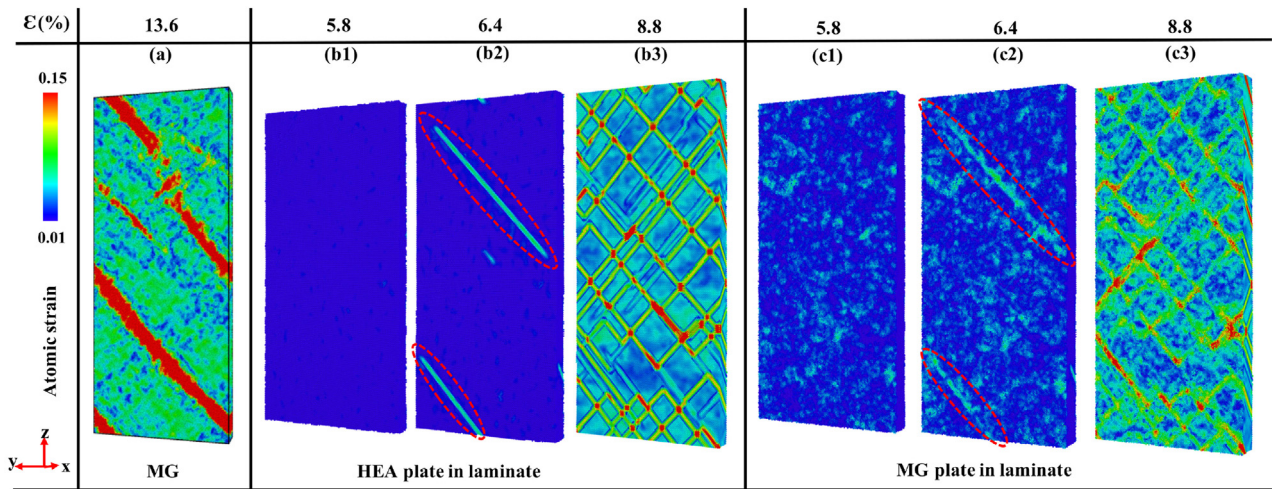
Fig. 9. Shear strain distribution in (a) the free-standing MG plate (b) the HEA plates of the MG-HEA laminate (c) the MG plates of the MG-HEA laminate during uniaxial tension at different strains. The atomic strain in the MG plate in the laminate shows a similar distribution as found in the crystalline plate. The red dashed circles display the locations of SBs in the HEA and MG plates in the laminate. (For interpretation of the references to color in this figure legend, the reader is referred to the web version of this article.)
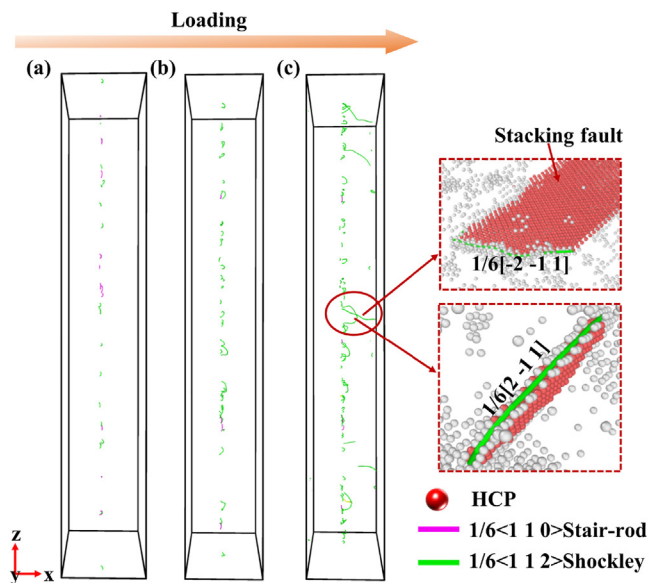

Fig. 10. Dislocation evolution at the interface of the MG-HEA laminate at different strain levels of (a) 0, (b) 5.8%, (c) 6.4%. The red circles highlight two representative stacking faults that are magnified in the two adjacent squared boxes. (For interpretation of the references to color in this figure legend, the reader is referred to the web version of this article.)

crystallization at the interface and the corresponding nucleation of Short Shockley partial dislocations and stair-rod dislocations takes place even before loading. Due to the pre-existent defects the plastic deformation in the laminate occurs at a lower stress or strain as compared to the free-standing HEA (Fig. 4). Furthermore, the decrease of activated crystallographic glide in the HEA plate in the laminate (see Fig. 6(b)) results from the corresponding cooperative and competing deformation in HEA and MG. Here, the plastic deformation is mediated by both, dislocations and SB formation and propagation, respectively.

The dislocation evolution during the deformation process is further investigated using DXA. The comparison between the dislocation density in the free-standing HEA plate and the HEA plate in the laminate is shown in Fig. 7. For the free-standing HEA, there are nearly no dislocations before reaching the yield strain of 10.4%,

while the number of dislocations increases rapidly up to a strain level 11.2% followed by a gradual increase until a strain level of 30%. Hence, the free-standing HEA behave like dislocation free material where a high yield strength is required for dislocation nucleation [53,61,62]. This is consistent with previous experimental work on compression tests of single crystalline nanopillars that showed catastrophic plastic collapse indicating that severe plastic deformation occurred in the pillars [62]. Similarly, here the sudden stress drop in the stress-strain curve of the free-standing HEA at the yield point correlates to the rapid increase in the dislocation density. For the HEA plate in the laminate, the dislocation density increases slower than for the free-standing HEA. Due to the inhibited slip of stacking faults in the HEA plate in the laminate, the emission of the dislocation at the yield point is much smaller than that found in the free-standing HEA. However, the increasing tendency of the dislocation density with strain in the plastic deformation stage is similar in both HEA plates, indicating that the brittle MG does not affect the ductility of the laminate.

In order to further analyze the dislocation evolution during the deformation process, the comparison of the dislocation structures in the free-standing HEA and the HEA plate in the laminate are investigated (see Fig. 8). Under tensile loading, just before yielding of the free-standing HEA (with a yield point of $\approx 10.8\%$) there are only a few and short dislocation lines but there are no slip events. After, yielding occurs through simultaneous nucleation of multiple partial dislocations that glide through the HEA, which results in the formation of deformation twins, as shown in Fig. 8(b) at the strain of 11.2%.

The larger number of dislocations acts as barrier to impede dislocation motion, resulting in further strain hardening of the free-standing HEA after a strain level of 11.2% (see Fig. 4). Besides, a significant amount of stacking faults occur through the HEA. It is well-known that the interactions among dislocations and TBs play an important role in determining the mechanical properties of single-phase FCC HEAs [63,64]. Multi-dislocation nodes and dislocation loops are found in the free-standing HEA (inset panels in Fig. 8(d)). The evolution of dislocations is mainly attributed to relaxation of a very large stress (approaching the theoretical value) at the yield point. The higher dislocation density and more dislocation loops act as barrier to further dislocation mobility.

For the HEA plate in the laminate, the short Shockley partial dislocations concentrate upon low strain (strain level of 5.8%, Fig. 8(e)). With further increasing strain, because of the initial low

number of dislocations and shorter slip distances, there is a weak interaction between dislocations while their propagation is confined by the MG plate, resulting in shorter and incomplete dislocations even at high strains. This indicates that the co-deformation of glass and crystalline phases inhibits the dislocations nucleation and propagation in the HEA plate, which leads to the decreased strength and enhanced plasticity for the MG-HEA laminate.

The crystallographic orientation plays an important role in the microstructure and mechanical properties for single crystals. For comparison, a new laminate model was constructed with a single crystal FCC HEA plate with a different crystallographic orientation of x (1 1 0), y (−1 1 0), and z (0 0 1) and deformed following the same procedure. Although there are same small differences in the stress-strain curves of the two laminates, overall there are no significant differences in their interfacial properties and the related deformation behaviors (for more information please consider the Supplementary Materials, Sec. S1).

5.2. Deformation mechanism of the MG

In order to highlight the differences between the deformation mechanisms of the free-standing MG plate and the MG layer in laminate, the atomic shear strain is depicted in Fig. 9. The plastic deformation in the free-standing MG is confined to one single SB that is usual for monolithic MGs (see Fig. 9(a)) [65,66]. This SB mediates the plastic deformation across the sample. However, the deformation behavior of the MG plate changes completely when it is confined between HEA plates (see Fig. 9(c)). Atomic shear strain diagrams of the glassy and crystalline plates at the different strain levels are depicted in Fig. 9(b) and (c). At a strain of 5.8%, there is no phase transformation in the crystalline plate. At the same time, STZs activate homogeneously in the glassy plate, mostly at the glass-crystalline interface with weakly bonded atoms and lower activation barriers [21]. With increasing strain, the phase transformation from FCC to HCP structure results in the formation of more stacking faults in the crystalline plate. Additionally, apparent STZs occur at the glass-crystalline interface along the position of the stacking faults, as shown in the red dashed circles (see Fig. 9(b2) and (c2)). More details on the relation between dislocations dynamics and STZs nucleation at the interface are provided in the Supplementary Materials, Sec. S2. This indicates that the deformation in the crystalline plate biases the STZ activation to regions near the glass-crystalline interface at lower strains. Concurrently, weakly bonded atoms at the interface reduce also the activation barrier for dislocation nucleation and propagation as manifested by a lower stress/strain at the onset of yielding of the MG-HEA laminate. The continuous nucleation and propagation of dislocations across the crystalline plate generates network-like STZs along the stacking faults and the formation of embryonic SBs [67](see Fig. 9(b3) and (c3)). These dislocations are blocked by the glassy plate while the stress at the dislocation tip triggers in turn the activation of new STZs at the glass-crystalline interface. Nevertheless, the SB nuclei cannot mature into extended defects, resulting in homogeneous deformation of the glassy plate. A pattern of multiple SBs intersecting each other can be seen in Fig. 9(c). Moreover, this competing deformation mechanism is the reason for the observed reduction of the dislocation density in the crystalline plate. In short, STZ activation and the formation of SBs in the MG plate are controlled by the formation of SFs and defects in the HEA plate.

6. Interface-related deformation phenomena

Finally, we analyze the relationship between the dislocation nucleation and evolution and the microstructure at the glass-crystalline interface during deformation in Fig. 10. Short Shockley partial dislocations and stair-rod dislocations exist at the inter-
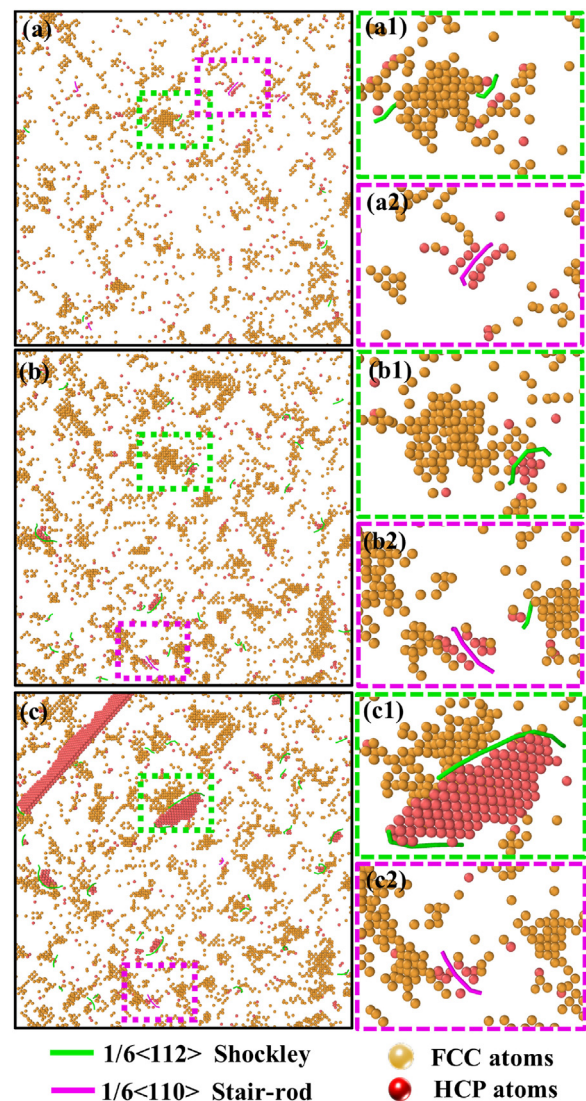

Fig. 11. The microstructure and dislocation distribution at the interface of MG-HEA laminate at different strain levels of (a) 0, (b) 5.8%, (c) 6.4%. (a1 and a2), (b1 and b2) and (c1 and c2) are the corresponding magnifications of the dashed squares in (a), (b) and (c). The atoms of the HEA plate and the glassy phase atoms of the MG plate are deleted for a better visualization of dislocations and nanocrystallites nucleation.

face even before loading due to the partial crystallization and the formation of nano-crystallites (Fig. 10(a)). During deformation, the dislocation density increases with further crystallization of the MG plate via stress-induced viscous flow [49,68]. However, the Shockley partial dislocation and stair-rod dislocations do not evolve until an applied strain of 6.4% (see Fig. 10(b)). Beyond a strain of 6.4 %, the dislocations propagate across the crystalline plate, as shown in Fig. 10(c). In addition, stacking faults are generated at this strain level. Once the defects start to propagate, the crystallization process at the interface stops and no other partial dislocations nucleate.

Deformation-induced crystallization of amorphous phases has been reported previously [31,69–71]. Besides, an increasing defect density is observed at the glass-crystalline interface (see Fig. 11), which is attributed to local composition fluctuations and microstructural changes from FCC to HCP (Fig. 11(a1, a2), (b1, b2) and (c1, c2)). HCP nucleation in the glassy plate induces the nucleation of short Shockley partial dislocations and stair-rod dislocations. The Shockley partial dislocations form around the nanocrys-

tals (Fig. 11(a1, b1, c1)) while stair-rod dislocations nucleate between two crystalline layers (Fig. 11(a2, b2, c2)). Interface crystallization accelerates with further increasing applied strain up to a level of 6.4%, and the density of both types of dislocations in the HEA plate increases. This indicates that the earlier yielding of the MG-HEA laminate inherently originates from the local atomic rearrangements and microstructural changes induced by the inhomogeneous stress redistribution at the interface.

7. Conclusions

In this work, MD simulations were employed to reveal the competing deformation mechanisms of MG-HEA nanolaminates. The main findings are summarized as follows:

(1) Glass-Crystalline interface: The relaxation of the residual stresses at the interface leads to crystallization via stress-induced viscous flow and formation of nanocrystallites in the MG plate distributed along the interface. Microstructural changes from FCC to HCP induce the nucleation of short Shockley partial dislocations at the interface. Additionally, interface crystallization accelerates under tensile loading and the density of Shockley partial dislocations increases, but they do not develop until the yield point.
(2) Confinement effects on the HEA plate: The HEA plate in the laminate exhibits no deformation twinning during tensile loading. Short Shockley partial dislocations due to the stress misfit and crystallization nucleate at the interface even before loading. The dislocations cause an earlier yielding of the MG-HEA laminate. Moreover, the nucleation and propagation of dislocations are inhibited by the MG plate resulting in a significantly lower dislocation density.
(3) Confinement effects on the MG plate: The deformation mechanism in the HEA plate controls the strain localization in the MG plate. Stacking faults and dislocations are absorbed into the MG plate via slip transfer across the glass-crystalline interface. Strain concentration at the location of slip triggers the activation of STZs in the glassy plate along the dislocation line. Consequently, network-like SBs form along the SFs, hindering the formation of a dominant SB. In conclusion, MG-HEA nanolaminates show exceptional strength and enhanced ductility outperforming monolithic MG. The design concept of MG-HEA laminates offers the flexibility to systematically tune their strength and ductility and, in the end, may allow to overcome the typical strength-ductility trade-off.

Declaration of Competing Interest

The authors have no competing interests to declare

Acknowledgments

Supplementary material

Supplementary material associated with this article can be found, in the online version, at doi:10.1016/j.actamat.2022.118191.

References

[1] J.W. Yeh, Alloy design strategies and future trends in high-entropy alloys, JOM 65 (12) (2013) 1759–1771.
[2] Z.P. Lu, H. Wang, M.W. Chen, I. Baker, J.W. Yeh, C.T. Liu, T.G. Nieh, An assessment on the future development of high-entropy alloys: summary from a recent workshop, Intermetallics 66 (2015) 67–76.
[3] E.P. George, D. Raabe, R.O. Ritchie, High-entropy alloys, Nat. Rev. Mater. 4 (8) (2019) 515–534.
[4] C.Y. Hsu, J.W. Yeh, S.K. Chen, T.T. Shun, Wear resistance and high-temperature compression strength of Fcc CuCoNiCrAl$_{0.5}$Fe alloy with boron addition, Metall. Mater. Trans. a 35 (5) (2004) 1465–1469.
[5] W.R. Zhang, P.K. Liaw, Y. Zhang, Science and technology in high-entropy alloys, Sci. China Mater. 61 (1) (2018) 2–22.
[6] D.B. Miracle, J.D. Miller, O.N. Senkov, C. Woodward, M.D. Uchic, J. Tiley, Exploration and development of high entropy alloys for structural applications, Entropy 16 (1) (2014) 494–525.
[7] J.W. Yeh, S.K. Chen, S.J. Lin, J.Y. Gan, T.S. Chin, T.T. Shun, C.H. Tsau, S.Y. Chang, Nanostructured high-entropy alloys with multiple principal elements: novel alloy design concepts and outcomes, Adv. Eng. Mater. 6 (5) (2004) 299–303.
[8] A.M. Manzoni, U. Glatzel, New multiphase compositionally complex alloys driven by the high entropy alloy approach, Mater. Charact. 147 (2019) 512–532.
[9] Q.L. Li, S. Zhao, B.Q. Li, Y.Q. Zhu, C.Z. Wang, Y.F. Lan, T.D. Xia, A novel modifier on the microstructure and mechanical properties of Al-7Si alloys, Mater. Lett. 251 (2019) 156–160.
[10] J. Chen, P. Niu, T. Wei, L. Hao, Y. Liu, X. Wang, Y. Peng, Fabrication and mechanical properties of AlCoNiCrFe high-entropy alloy particle reinforced Cu matrix composites, J. Alloys Compd. 649 (2015) 630–634.
[11] Z. Tan, L. Wang, L. Xue, P. Zhang, T. Cao, X. Cheng, High-entropy alloy particle reinforced Al-based amorphous alloy composite with ultrahigh strength prepared by spark plasma sintering, Mater. Des. 109 (2016) 219–226.
[12] W.H. Wang, C. Dong, C. Shek, Bulk metallic glasses, Mater. Sci. Eng. 44 (2–3) (2004) 45–89.
[13] C.A. Schuh, T.C. Hufnagel, U. Ramamurty, Mechanical behavior of amorphous alloys, Acta Mater. 55 (12) (2007) 4067–4109.
[14] J. Eckert, J. Das, S. Pauly, C. Duhamel, Mechanical properties of bulk metallic glasses and composites, J. Mater. Res. 22 (2) (2007) 285–301.
[15] S. Scudino, H.S. Shahabi, M. Stoica, I. Kaban, B. Escher, U. Kühn, G. Vaughan, J. Eckert, Structural features of plastic deformation in bulk metallic glasses, Appl. Phys. Lett. 106 (3) (2015) 031903.
[16] A. Sergueeva, N. Mara, J. Kuntz, E. Lavernia, A. Mukherjee, Shear band formation and ductility in bulk metallic glass, Philos. Mag. 85 (23) (2005) 2671–2687.
[17] T. Nieh, T. Barbee, J. Wadsworth, Tensile properties of a free-standing Cu/Zr nanolaminate (or compositionally-modulated thin film), Scr. Mater. 41 (9) (1999) 929–935.
[18] B. Arman, C. Brandl, S. Luo, T. Germann, A. Misra, T. Çağin, Plasticity in Cu (111)/Cu$_{46}$Zr$_{54}$ glass nanolaminates under uniaxial compression, J. Appl. Phys. 110 (4) (2011) 043539.
[19] B. Cheng, J.R. Trelewicz, Mechanistic coupling of dislocation and shear transformation zone plasticity in crystalline-amorphous nanolaminates, Acta Mater. 117 (2016) 293–305.
[20] G. He, J. Eckert, W. Löser, L. Schultz, Novel Ti-base nanostructure-dendrite composite with enhanced plasticity, Nat. Mater. 2 (1) (2003) 33–37.
[21] D. Şopu, M. Stoica, J. Eckert, Deformation behavior of metallic glass composites reinforced with shape memory nanowires studied via molecular dynamics simulations, Appl. Phys. Lett. 106 (21) (2015) 211902.
[22] D. Şopu, X. Yuan, F. Moitzi, M. Stoica, J. Eckert, Structure-property relationships in shape memory metallic glass composites, Materials 12 (9) (2019) 1419.
[23] W. Guo, E. Jägle, J. Yao, V. Maier, S. Korte-Kerzel, J.M. Schneider, D. Raabe, Intrinsic and extrinsic size effects in the deformation of amorphous CuZr/nanocrystalline Cu nanolaminates, Acta Mater. 80 (2014) 94–106.
[24] D.C. Hofmann, J.Y. Suh, A. Wiest, G. Duan, M.L. Lind, M.D. Demetriou, W.L. Johnson, Designing metallic glass matrix composites with high toughness and tensile ductility, Nature 451 (7182) (2008) 1085–1089.
[25] Y. Wang, J. Li, A.V. Hamza, T.W. Barbee, Ductile crystalline-amorphous nanolaminates, Proc. Natl. Acad. Sci. 104 (27) (2007) 11155–11160.
[26] S. Yamamoto, Y.J. Wang, A. Ishii, S. Ogata, Atomistic design of high strength crystalline-amorphous nanocomposites, Mater. Trans. 54 (9) (2013) 1592–1596.
[27] J.R. Greer, J.T.M. De Hosson, Plasticity in small-sized metallic systems: intrinsic versus extrinsic size effect, Prog. Mater. Sci. 56 (6) (2011) 654–724.
[28] D. Şopu, K. Albe, J. Eckert, Metallic glass nanolaminates with shape memory alloys, Acta Mater. 159 (2018) 344–351.
[29] X.Y. Zhou, H.H. Wu, J.H. Zhu, B. Li, Y. Wu, Plastic deformation mechanism in crystal-glass high entropy alloy composites studied via molecular dynamics simulations, Compos. Commun. 24 (2021) 100658.
[30] G. Wu, S. Balachandran, B. Gault, W. Xia, C. Liu, Z. Rao, Y. Wei, S. Liu, J. Lu, M. Herbig, W. Lu, G. Dehm, Z. Li, D. Raabe, Crystal-glass high-entropy nanocomposites with near theoretical compressive strength and large deformability, Adv. Mater. 32 (34) (2020) 2002619.

[31] W. Guo, J. Yao, E.A. Jägle, P.P. Choi, M. Herbig, J.M. Schneider, D. Raabe, Deformation induced alloying in crystalline-metallic glass nano-composites, Mater. Sci. Eng. A 628 (2015) 269–280.

[32] W.P. Wu, D. Șopu, J. Eckert, Molecular dynamics study of the nanoindentation behavior of $Cu_{64}Zr_{36}$/Cu amorphous/crystalline nanolaminate composites, Materials 14 (11) (2021) 2756.

[33] S. Feng, L. Li, K. Chan, L. Qi, L. Zhao, L. Wang, R. Liu, Control of shear band dynamics in $Cu_{50}Zr_{50}$ metallic glass by introducing amorphous-crystalline interfaces, J. Alloys Compd. 770 (2019) 896–905.

[34] J. Jordan, K.I. Jacob, R. Tannenbaum, M.A. Sharaf, I. Jasiuk, Experimental trends in polymer nanocomposites—Areview, Mater. Sci. Eng. A 393 (1–2) (2005) 1–11.

[35] J. Zhang, G. Liu, S. Lei, J. Niu, J. Sun, Transition from homogeneous-like to shear-band deformation in nanolayered crystalline Cu/amorphous Cu-Zr micropillars: intrinsic vs. extrinsic size effect, Acta Mater. 60 (20) (2012) 7183–7196.

[36] J. Zhang, G. Liu, J. Sun, Self-toughening crystalline Cu/amorphous Cu-Zr nanolaminates: deformation-induced devitrification, Acta Mater. 66 (2014) 22–31.

[37] W. Guo, E.A. Jägle, P.P. Choi, J. Yao, A. Kostka, J.M. Schneider, D. Raabe, Shear-induced mixing governs codeformation of crystalline-amorphous nanolaminates, Phys. Rev. Lett. 113 (3) (2014) 035501.

[38] B. Cheng, J.R. Trelewicz, Design of crystalline-amorphous nanolaminates using deformation mechanism maps, Acta Mater. 153 (2018) 314–326.

[39] S. Plimpton, Fast parallel algorithms for short-range molecular dynamics, J. Comput. Phys. 117 (1) (1995) 1–19.

[40] D. Farkas, A. Caro, Model interatomic potentials for Fe-Ni-Cr-Co-Al high-entropy alloys, J. Mater. Res. 35 (22) (2020) 3031–3040.

[41] J. Cieslak, J. Tobola, K. Berent, M. Marciszko, Phase composition of Al_xFeNiCrCo high entropy alloys prepared by sintering and arc-melting methods, J. Alloys Compd. 740 (2018) 264–272.

[42] A. Sharma, S.A. Deshmukh, P.K. Liaw, G. Balasubramanian, Crystallization kinetics in Al_xCrCoFeNi ($0 \leq x \leq 40$) high-entropy alloys, Scr. Mater. 141 (2017) 54–57.

[43] S. Mishra, K.V. Reddy, S. Pal, Impact of crystalline–amorphous interface on shock response of metallic glass $Al_{90}Sm_{10}$/crystalline al nanolaminates, Appl. Phys. A 127 (10) (2021) 1–13.

[44] K.V. Reddy, C. Deng, S. Pal, Dynamic characterization of shock response in crystalline-metallic glass nanolaminates, Acta Mater. 164 (2019) 347–361.

[45] A. Stukowski, Visualization and analysis of atomistic simulation data with OVITO-the open visualization tool, Model. Simul. Mat. Sci. Eng. 18 (1) (2009) 015012.

[46] A. Stukowski, Structure identification methods for atomistic simulations of crystalline materials, Model. Simul. Mat. Sci. Eng. 20 (4) (2012) 045021.

[47] B. Devincre, L.P. Kubin, Mesoscopic simulations of dislocations and plasticity, Mater. Sci. Eng. A 234 (1997) 8–14.

[48] D. Faken, H. Jónsson, Systematic analysis of local atomic structure combined with 3D computer graphics, Comput. Mater. Sci. 2 (2) (1994) 279–286.

[49] Y. Wang, D. Kiener, X. Liang, J. Bian, K. Wu, J. Zhang, G. Liu, J. Sun, Constituent constraining effects on the microstructural evolution, ductility, and fracture mode of crystalline/amorphous nanolaminates, J. Alloys Compd. 768 (2018) 88–96.

[50] Y. Mao, J. Li, Y.C. Lo, X. Qian, E. Ma, Stress-driven crystallization via shear-diffusion transformations in a metallic glass at very low temperatures, Phys. Rev. B 91 (21) (2015) 214103.

[51] Z. Yan, K. Song, Y. Hu, F. Dai, Z. Chu, J. Eckert, Localized crystallization in shear bands of a metallic glass, Sci. Rep. 6 (1) (2016) 1–7.

[52] H. Bi, A. Inoue, F. Han, Y. Han, F. Kong, S. Zhu, E. Shalaan, F.A. Marzouki, A. Greer, Novel deformation-induced polymorphic crystallization and softening of Al-based amorphous alloys, Acta Mater. 147 (2018) 90–99.

[53] P.S. Phani, K.E. Johanns, G. Duscher, A. Gali, E.P. George, G.M. Pharr, Scanning transmission electron microscope observations of defects in as-grown and pre-strained mo alloy fibers, Acta Mater. 59 (5) (2011) 2172–2179.

[54] J. Li, Q. Fang, B. Liu, Y. Liu, Y. Liu, Mechanical behaviors of AlCrFeCuNi high-entropy alloys under uniaxial tension via molecular dynamics simulation, RSC Adv. 6 (80) (2016) 76409–76419.

[55] A. Ulvestad, M. Welland, W. Cha, Y. Liu, J. Kim, R. Harder, E. Maxey, J. Clark, M. Highland, H. You, P. Zapol, S.O. Hruszkewycz, G.B. Stephenson, Three-dimensional imaging of dislocation dynamics during the hydriding phase transformation, Nat. Mater. 16 (5) (2017) 565–571.

[56] Q. Fang, Y. Chen, J. Li, C. Jiang, B. Liu, Y. Liu, P.K. Liaw, Probing the phase transformation and dislocation evolution in dual-phase high-entropy alloys, Int. J. Plast. 114 (2019) 161–173.

[57] L. Daróczi, T.Y. Elrasasi, T. Arjmandabasi, L.Z. Tóth, B. Veres, D.L. Beke, Change of acoustic emission characteristics during temperature induced transition from twinning to dislocation slip under compression in polycrystalline Sn, Materials 15 (1) (2022) 224.

[58] S.J. Turneaure, P. Renganathan, J. Winey, Y. Gupta, Twinning and dislocation evolution during shock compression and release of single crystals: real-time X-ray diffraction, Phys. Rev. Lett. 120 (26) (2018) 265503.

[59] J. Gao, Y. Huang, D. Guan, A.J. Knowles, L. Ma, D. Dye, W.M. Rainforth, Deformation mechanisms in a metastable beta titanium twinning induced plasticity alloy with high yield strength and high strain hardening rate, Acta Mater. 152 (2018) 301–314.

[60] Y. Zhu, J. Narayan, J. Hirth, S. Mahajan, X. Wu, X. Liao, Formation of single and multiple deformation twins in nanocrystalline fcc metals, Acta Mater. 57 (13) (2009) 3763–3770.

[61] C. Chisholm, H. Bei, M. Lowry, J. Oh, S.S. Asif, O. Warren, Z. Shan, E.P. George, A.M. Minor, Dislocation starvation and exhaustion hardening in Mo alloy nanofibers, Acta Mater. 60 (5) (2012) 2258–2264.

[62] H. Bei, S. Shim, G.M. Pharr, E.P. George, Effects of pre-strain on the compressive stress–strain response of mo-alloy single-crystal micropillars, Acta Mate. 56 (17) (2008) 4762–4770.

[63] M.J. Jang, S.H. Joo, C.W. Tsai, J.W. Yeh, H.S. Kim, Compressive deformation behavior of CrMnFeCoNi high-entropy alloy, Met. Mater. Int. 22 (6) (2016) 982–986.

[64] X. Xu, P. Liu, Z. Tang, A. Hirata, S. Song, T. Nieh, P. Liaw, C. Liu, M. Chen, Transmission electron microscopy characterization of dislocation structure in a face-centered cubic high-entropy alloy $Al_{0.1}$CoCrFeNi, Acta Mater. 144 (2018) 107–115.

[65] C. Hays, C. Kim, W.L. Johnson, Microstructure controlled shear band pattern formation and enhanced plasticity of bulk metallic glasses containing in situ formed ductile phase dendrite dispersions, Phys. Rev. Lett. 84 (13) (2000) 2901.

[66] D. Șopu, Y. Ritter, H. Gleiter, K. Albe, Deformation behavior of bulk and nanostructured metallic glasses studied via molecular dynamics simulations, Phys. Rev. B 83 (10) (2011) 100202.

[67] J. Li, H. Chen, H. Feng, Q. Fang, Y. Liu, F. Liu, H. Wu, P.K. Liaw, Microstructure evolution and deformation mechanism of amorphous/crystalline high-entropy-alloy composites, J. Mater. Sci. Technol. 54 (2020) 14–19.

[68] Y.Q. Wang, J.Y. Zhang, X.Q. Liang, K. Wu, G. Liu, J. Sun, Size-and constituent-dependent deformation mechanisms and strain rate sensitivity in nanolaminated crystalline Cu/amorphous Cu-Zr films, Acta Mater. 95 (2015) 132–144.

[69] G.J. Fan, M.X. Quan, Z. Hu, W. Löser, J. Eckert, Deformation-induced microstructural changes in $Fe_{40}Ni_{40}P_{14}B_6$ metallic glass, J. Mater. Res. 14 (9) (1999) 3765–3774.

[70] Q. Cao, J. Li, Y. Zhou, A. Horsewell, J. Jiang, Effect of rolling deformation on the microstructure of bulk $Cu_{60}Zr_{20}Ti_{20}$ metallic glass and its crystallization, Acta Mater. 54 (16) (2006) 4373–4383.

[71] G. Li, Y.Q. Wang, L.M. Wang, Y.P. Gao, R. Zhang, Z.J. Zhan, L.L. Sun, J. Zhang, W.K. Wang, Wear behavior of bulk $Zr_{41}Ti_{14}Cu_{12.5}Ni_{10}Be_{22.5}$ metallic glasses, J. Mater. Res. 17 (8) (2002) 1877–1880.